Sequential prediction of transverse crack paths in CFRP composites via a deep learning approach

Fengtian Shi[a], Siqing Liu[a], Xin Yan[a, *], Wuxiang Zhang[a, *], Xilun Ding[a]

[a]*School of Mechanical Engineering and Automation, BeihangUniversity, 37XueyuanRoad, Beijing 100191, China*

Transverse cracking is one of the earliest damage modes in carbon fiber-reinforced polymer (CFRP) composites under transverse or complex loading, leading to stiffness degradation and reduced fatigue life. Its initiation and early propagation occur at the microscale and are strongly influenced by random fiber distributions and local stress concentrations. However, transverse crack propagation cannot be fully characterized within a single microstructural window, owing to the combined effects of the local fiber arrangement and crack state inheritance from the preceding region. To address this challenge, a physics guided deep learning framework is developed for sequential prediction of transverse crack paths in CFRP composites. Specifically, the framework directly predicts crack paths from microstructural images and incorporates the predicted crack segment as the initial crack information for the subsequent prediction window, thereby enabling sequential prediction across neighboring regions. An attention enhanced encoder decoder network is employed to capture multiscale features of crack evolution, while physical guidance derived from phase-field fracture analysis is incorporated to improve the consistency of the predicted paths. Compared with phase-field model results, the proposed framework accurately reconstructs transverse crack paths in extended microstructural regions with a prediction accuracy of 93.8%. This study provides an efficient surrogate model for sequential transverse crack path prediction and multiscale damage analysis of CFRP composites.

Keywords: Carbon Fiber-reinforced polymer, Deep learning, Composite materials, Transverse crack path prediction, Phase field simulation.

*Corresponding authors.

E-mail address: xin_yan@buaa.edu.cn (Xin Yan), zhangwuxiang@buaa.edu.cn (Wuxiang Zhang)

1.Introduction

Carbon fiber-reinforced polymer composites (CFRPs) have been widely used in load-bearing structures in aerospace, transportation, and wind energy applications because of their high specific strength, high specific stiffness, and excellent structural tailorability [1]. In engineering practice, CFRP components are usually manufactured as multidirectional laminates composed of 0°, ±45°, and 90° plies to satisfy complex service requirements, including axial tension and compression, in-plane shear, and transverse loading. Among these plies, the 90° ply is loaded perpendicular to the fiber direction. Its transverse mechanical response is therefore governed mainly by the relatively weak polymer matrix and the fiber/matrix interface. As a result, transverse matrix cracking is often one of the earliest damage modes in CFRP laminates under tensile, fatigue, or complex loading conditions [2,4]. Previous studies have shown that transverse cracks can reduce laminate stiffness, promote delamination, and accelerate subsequent damage evolution, including fiber fracture, thereby degrading the load-bearing capacity and fatigue life of composite structures [3,6]. Accurate prediction of transverse crack initiation and propagation paths is therefore essential for damage-tolerant design and safety assessment of CFRP composite structures.

Despite its engineering importance, transverse crack prediction in CFRPs remains challenging because of the multiscale and stochastic nature of microstructural damage. Transverse cracks usually initiate in matrix-rich regions between neighboring fibers or near fiber/matrix interfaces, and their early propagation may occur at length scales of only tens of micrometers [2,7,8]. Microstructural factors, such as fiber spatial distribution, local fiber spacing, interfacial properties, and void defects, jointly affect local stress concentrations and crack-driving forces. These factors introduce substantial uncertainty into both crack initiation sites and propagation paths [8-10]. Conventional experimental techniques, including microscopic observation, acoustic emission monitoring, digital image correlation, and X-ray computed tomography, can provide valuable information for damage identification and characterization [2,7,11,12]. However, these methods are still limited in capturing early-stage microcracks with small openings because of constraints related to spatial resolution, testing cost, signal-to-noise ratio, and offline characterization [11,12]. Therefore, an efficient crack path prediction method directly based on microstructural information is needed to clarify transverse cracking mechanisms and support multiscale failure analysis.

The finite element method and its extensions have been extensively used to investigate microscale damage evolution in composite materials. By constructing representative volume elements containing fibers, matrix, and interfaces, and by incorporating cohesive zone models, extended finite element methods, phase-field approaches, or discrete element methods, researchers can simulate matrix cracking, interfacial debonding, and crack propagation processes [13–15]. These physics-based

approaches provide detailed stress fields and damage evolution information, which are crucial for understanding the mechanisms of transverse cracking. However, when random fiber distributions, variations in fiber volume fraction, and large numbers of microstructural samples are considered, high-fidelity simulations become computationally expensive [15,16]. In addition, the predicted crack paths are often sensitive to mesh discretization, damage parameters, and boundary conditions [17]. These limitations restrict the use of physics-based simulations in large-scale parametric studies and rapid prediction of crack evolution.

Recently, data-driven approaches, particularly deep learning methods, have emerged as promising alternatives for composite damage prediction. These methods can learn nonlinear mappings between microstructural features and fracture responses from simulation or experimental data, thereby significantly reducing the computational cost of repeated analyses. Existing studies have applied deep learning techniques to predict effective properties, stress fields, crack locations, and crack patterns in fiber-reinforced composites [10,18-25]. For example, Zhang et al. proposed an end-to-end framework that integrates microstructure images and physical field information and reformulates crack path prediction as a pixel-wise segmentation problem [18]. Peng et al. developed a 3D TransU-Net framework combined with transfer learning for efficient prediction of multicomponent stress fields in fiber-reinforced composites under different load paths [19]. Gu et al. coupled discrete element simulations with deep learning models to predict transverse cracks in unidirectional glass fiber-reinforced polymer composites [20]. Wang et al. proposed a two-stage deep learning framework to predict crack patterns and mechanical properties of unidirectional composites with void defects [10]. These studies demonstrate the capability of deep learning models to capture complex relationships between microstructural characteristics and damage responses.

Although significant progress has been achieved, current data-driven methods still face critical limitations in predicting sequential transverse crack propagation in CFRPs. Most existing approaches focus on crack prediction within a single representative volume element or an isolated microstructural region, while the inherent sequential nature of crack propagation across neighboring regions is often neglected [10,18,20,21]. Moreover, several methods rely on intermediate physical fields, such as stress distributions, which limits their applicability in fast prediction scenarios [19,25]. More importantly, transverse crack propagation exhibits strong path dependence: an existing crack modifies the local mechanical environment and affects the subsequent crack growth direction. If this sequential dependency is ignored, independent predictions in adjacent microstructural units may form disconnected information islands that cannot be assembled into a physically consistent crack path.

To overcome these limitations, this study proposes a deep learning-based

sequential prediction framework for transverse crack path prediction in CFRP composites. The proposed framework takes microstructures with random fiber distributions as input and directly establishes the mapping between microstructural features and crack paths. More importantly, previously propagated crack information is introduced as a bridging variable between adjacent prediction units, enabling information transfer and explicitly capturing the sequential dependency of crack propagation. In the proposed model, a ResNet encoder is used for robust feature extraction [26], and a U-Net-based decoder with attention mechanisms is adopted to recover crack paths while preserving multiscale spatial information [27,28]. The predicted crack paths are evaluated using the structural similarity index and an improved Hausdorff-distance-based crack detection algorithm [29,30]. Through this strategy, the proposed method enables sequential reconstruction of transverse crack paths from local microstructural units to extended microstructural regions, providing an efficient data-driven tool for transverse cracking analysis, microstructural damage evolution modeling, and rapid structural assessment of CFRP composites.

2. Phase-field modeling and microstructure generation

2.1 Microstructure generation

Two-dimensional microstructural windows were constructed to represent the transverse cross-section of a unidirectional CFRP lamina. As shown in Fig. 1(a), a non-periodic square window was adopted instead of a conventional periodic RVE, so that the crack segment predicted in the current window can be transferred to the adjacent window during sequential prediction. A displacement load was applied to the upper boundary to reproduce the transverse tensile state of the 90° ply in a laminate, while the remaining boundaries were constrained to suppress rigid-body motion and maintain a stable loading configuration.

Each microstructural window was defined as a $30\mu m \times 30\mu m$ square domain, in which circular carbon fibers with a radius of $4\mu m$ were randomly distributed in the matrix. The window size was selected to capture matrix crack initiation and early propagation while reducing the computational cost required for phase-field simulations and dataset generation. Therefore, the adopted window provides a compromise between microscale fracture representation and high-throughput data construction.

The random fiber distributions were generated using a spatial exclusion algorithm, as illustrated in Fig. 1(b). A fiber center was first sampled within the square domain, and the occupied fiber region together with its surrounding exclusion zone was removed from the admissible sampling space. Subsequent fiber centers were then sequentially generated in the remaining space until the prescribed fiber volume fraction was reached. This procedure prevents fiber overlap and avoids repeated rejection of invalid samples, thereby improving the efficiency of valid microstructure generation. Representative

generated microstructures are shown in Fig. 1(c). To improve the generalization capability of the deep learning model, the generated samples covered a fiber volume fraction range of 50–62%.

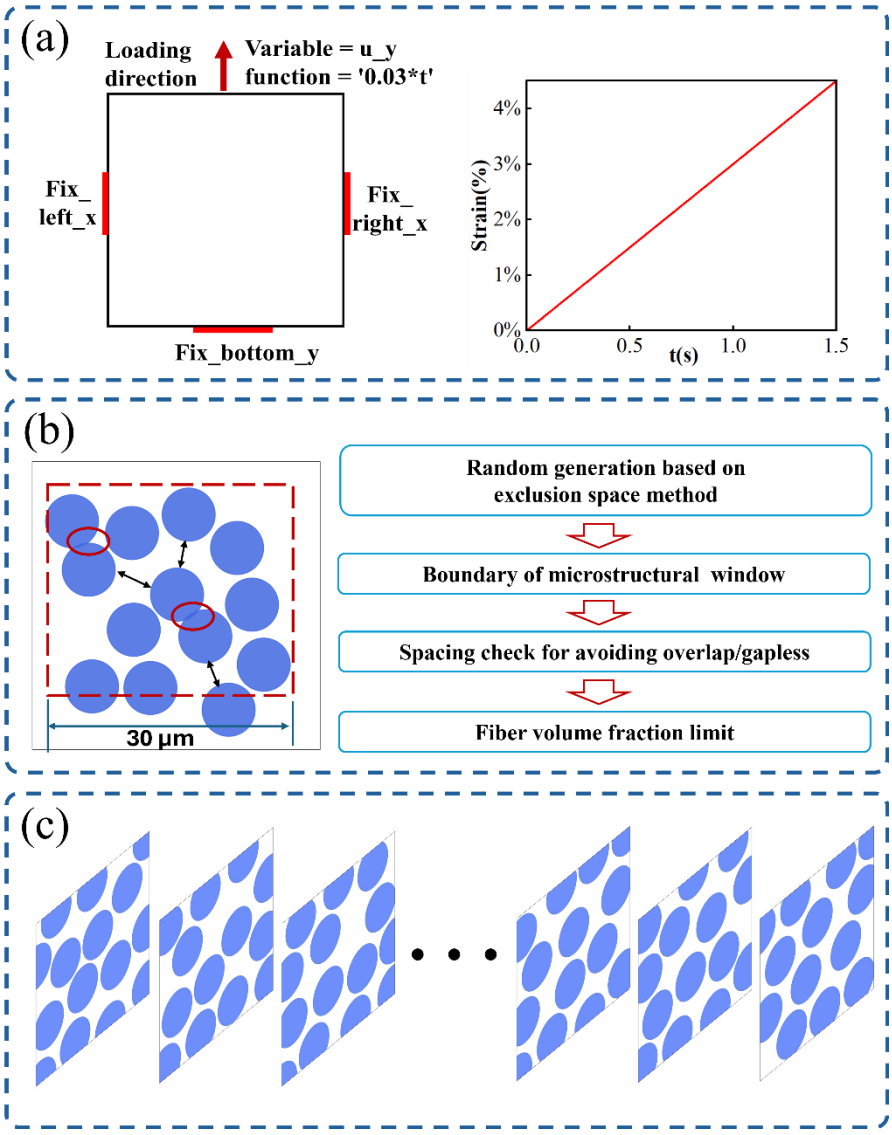

Fig. 1. Microstructure generation and loading configuration. (a) Non-periodic microstructural window with transverse displacement loading and boundary constraints. (b) Spatial exclusion algorithm for generating randomly distributed fibers. (c) Representative generated microstructures with different fiber volume fractions.

2.2 Phase-field model

The phase-field fracture model was employed to generate reference crack fields for supervised learning. Based on Griffith fracture theory, the total energy of a cracked solid is expressed as the sum of the elastic strain energy stored in the bulk domain and the fracture energy dissipated by newly formed crack surfaces. A scalar damage variable d is introduced to describe crack evolution, where d=0represents the intact material and d=1denotes complete failure. The total energy functional is written as [31,32]

$$F(u,d)=\int_{\Omega}\psi(\varepsilon,d)d\Omega+G_c\int_{\Gamma}d\Gamma \tag{1}$$

where u is the displacement vector, ε is the strain tensor, Ω is the solid domain, Γ is the crack surface, and G_c is the critical energy release rate [32].

To avoid nonphysical crack growth under compression, a stress-based spectral decomposition was adopted to separate the tensile and compressive contributions to the elastic energy density. The tensile and compressive energy densities are defined as [33]

$$\begin{cases}\psi_+=\dfrac{1}{2}\sigma_+:\varepsilon\\ \psi_-=\dfrac{1}{2}\sigma_-:\varepsilon\end{cases} \tag{2}$$

With

$$\sigma_+=P_+\sigma_0,\qquad \sigma_-=P_-\sigma_0,\qquad \sigma_0=C:\varepsilon \tag{3}$$

where C elastic stiffness tensor, σ_0 undamaged stress tensor, and P_+,P_- are the positive and negative projection operators obtained from the spectral decomposition of the undamaged stress tensor.

Only the tensile part of the elastic energy was degraded during crack evolution. The degraded elastic energy density is expressed as [32]

$$\psi(\varepsilon,d)=w(d)\psi_+(\varepsilon)+\psi_-(\varepsilon),\qquad w(d)=(1-d)^2 \tag{4}$$

where $w(d)$ is the degradation function. The sharp crack surface was regularized over the bulk domain, and the fracture surface energy was approximated as [32]

$$G_c\int_{\Gamma}d\Gamma\approx\frac{3G_c}{8l}\int_{\Omega}[d+l^2|\nabla d|^2]d\Omega \tag{5}$$

where l is the length-scale parameter controlling the width of the diffusive crack zone.

The degraded stress tensor and the material tangent used in the finite-element implementation can be written as

$$\sigma=\frac{\partial\psi}{\partial\varepsilon}=w(d)\sigma_+ +\sigma_- \tag{6}$$

$$J=\frac{\partial\sigma}{\partial\varepsilon}=(w(d)P_+ +P_-)C \tag{7}$$

To enforce damage irreversibility and prevent crack healing during unloading or local stress redistribution, a history variable H was introduced to record the maximum tensile energy density reached during loading [32]

$$H=\max_{\tau\in[0,t]}\psi_+(x,\tau) \tag{8}$$

where x denotes the spatial coordinate, t is the current loading time, τ is the historical loading variable within the interval $[0,t]$.

Substituting Eq. (4) and (5) into Eq. (1), the regularized energy functional becomes

$$F(u,d)=\int_{\Omega}[(1\text{-}d)^2H+\psi_-]+[\frac{3G_c}{8l}(d+l^2\nabla d\cdot\nabla d)]d\Omega \tag{9}$$

Since d is a non-conserved order parameter, its evolution is governed by a time-dependent phase-field kinetic equation

$$\frac{\partial d}{\partial t}=-L\frac{\delta F}{\delta d} \tag{10}$$

where L is the kinetic coefficient controlling the damage evolution rate. Taking the variational derivative of Eq. (9) gives

$$\frac{\partial d}{\partial t}=-L[(2d\text{-}2)H+\frac{3G_c}{8l}-\nabla\cdot\frac{3G_c l}{4}\nabla d)] \tag{11}$$

To prevent negative values of d and improve numerical stability, an obstacle term was further introduced. The corresponding barrier force and modified history variable are defined as:

$$f_{ba}=\frac{3G_c}{16l},\qquad H=\max_{0\sim t}(\psi_+,f_{ba}) \tag{12}$$

where f_{ba} denotes the barrier force associated with the obstacle constraint.

The governing equations were implemented in the finite-element framework of the Multiphysics Object-Oriented Simulation Environment (MOOSE). The simulated phase-field variable d was extracted and post-processed into crack-field labels for training and validating the subsequent deep learning model.

2.3 Phase-field fracture characteristics

Phase-field simulations were used to examine the fracture characteristics governing transverse crack evolution in the generated CFRP microstructures. Fig. 2(a) shows the field-averaged stress–strain response of a representative microstructural window under transverse tensile loading. The curve exhibits an initial nearly linear elastic stage, indicating that the microstructure remains largely intact. With increasing strain, the response reaches a peak stress, followed by a gradual stress reduction associated with matrix damage initiation and crack growth. The subsequent softening stage reflects progressive crack propagation and coalescence. Once a dominant transverse crack forms across the window, the load-carrying capacity degrades rapidly.

Stress-field and crack-field distributions at selected loading stages are shown in Fig. 2(b). Before crack initiation, tensile stress is localized in the matrix ligaments between closely spaced neighboring fibers, providing preferential sites for damage nucleation. After local damage occurs, stress in the cracked ligament is released, while stress concentrations develop near adjacent fiber gaps and crack tips. With further loading, isolated damaged regions extend and coalesce into a continuous transverse crack. The crack path is thus controlled by stress redistribution and the geometric constraints imposed by the surrounding fibers.

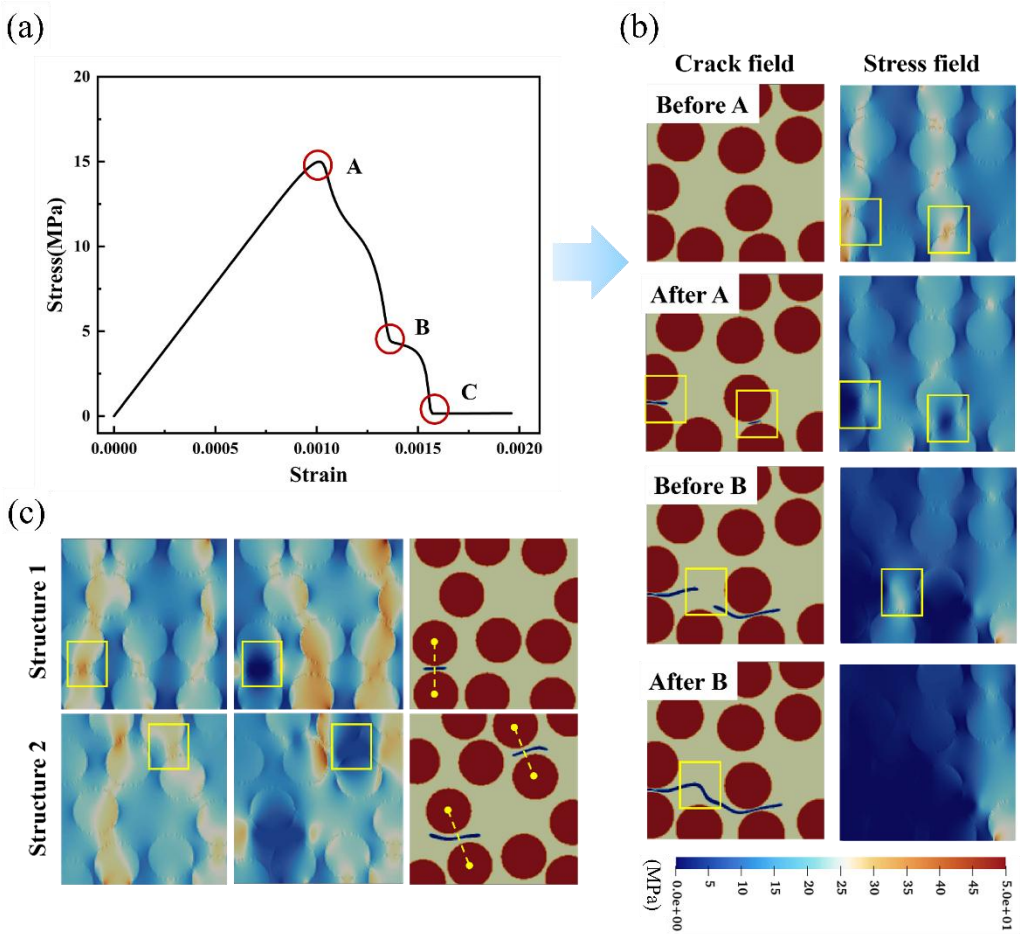

Fig. 2. Phase-field fracture results and analysis. (a) Mean stress–strain relationship of the field. (b) Distributions of crack phase field and stress field before and after crack initiation and propagation. (c) Influence of fiber distribution characteristics on crack initiation location.

Fig. 2(c) compares stress-field variations before and after crack initiation for different random fiber distributions. Although the initiation sites vary with the local microstructure, a consistent trend is observed: cracks tend to initiate in narrow matrix ligaments where tensile stress concentration is pronounced. These critical regions are typically located between neighboring fibers approximately aligned with the loading direction, where the matrix ligament is subjected to intensified transverse tension. This behavior confirms the strong influence of local fiber arrangement on crack nucleation and path selection.

Overall, transverse crack evolution is governed by local stress concentration, fiber spacing, and crack-induced stress redistribution. These observations provide the physical basis for the subsequent physics-guided deep learning framework, in which crack prediction is constrained by mechanically preferred cracking regions identified from the phase-field analysis.

3. PGNN model for predicting transverse crack paths

A physics guided neural network (PGNN) was developed to predict transverse crack paths in CFRP microstructures. The proposed framework learns the mapping between microstructural images and the corresponding crack fields obtained from phase field simulations. The prediction task is formulated as a pixelwise crack segmentation problem, in which the network outputs a single channel crack probability map with the same spatial resolution as the reference damage field.

Unlike methods that require stress, strain, or strain energy fields as additional network inputs, the present framework uses only microstructural images as input, while physical guidance is incorporated during training through geometry-based masks extracted from the same images. These masks are constructed according to the phase field observations in Section 2.3, which indicate that crack initiation is closely associated with local stress concentration, inter fiber spacing, the angle between the center-to-center line of neighboring fibers and the loading direction, and crack induced stress redistribution.

3.1 Data generation and preprocessing

The microstructure generation procedure described in Section 2.1 was used to construct randomly distributed CFRP microstructural windows. Each valid microstructure was submitted to the MOOSE phase field solver, and the final damage variable d was extracted as the reference crack field. The generated dataset consists of paired samples, where each sample contains a microstructural image and its corresponding phase field crack map.

The microstructural images were stored in RGB format with a spatial resolution of 512×512. Different colors were assigned to distinguish the fiber and matrix phases. The corresponding crack maps were obtained from the final phase field damage distributions and normalized as single channel images with the same spatial resolution. Pixels with high damage values represent cracked regions, whereas pixels with low damage values correspond to intact regions. Accordingly, the learning task is defined as predicting a single channel crack field from a three channel microstructural image.

During preprocessing, a fiber mask M_f was extracted from each microstructural image according to the color difference between the fiber and matrix phases. This mask identifies the fiber interiors and provides the basis for imposing the physical constraint that transverse matrix cracks should not penetrate fibers in the present model. Based on the extracted fiber mask, individual fiber centers were detected, and neighboring fiber pairs were determined according to their center-to-center distances.

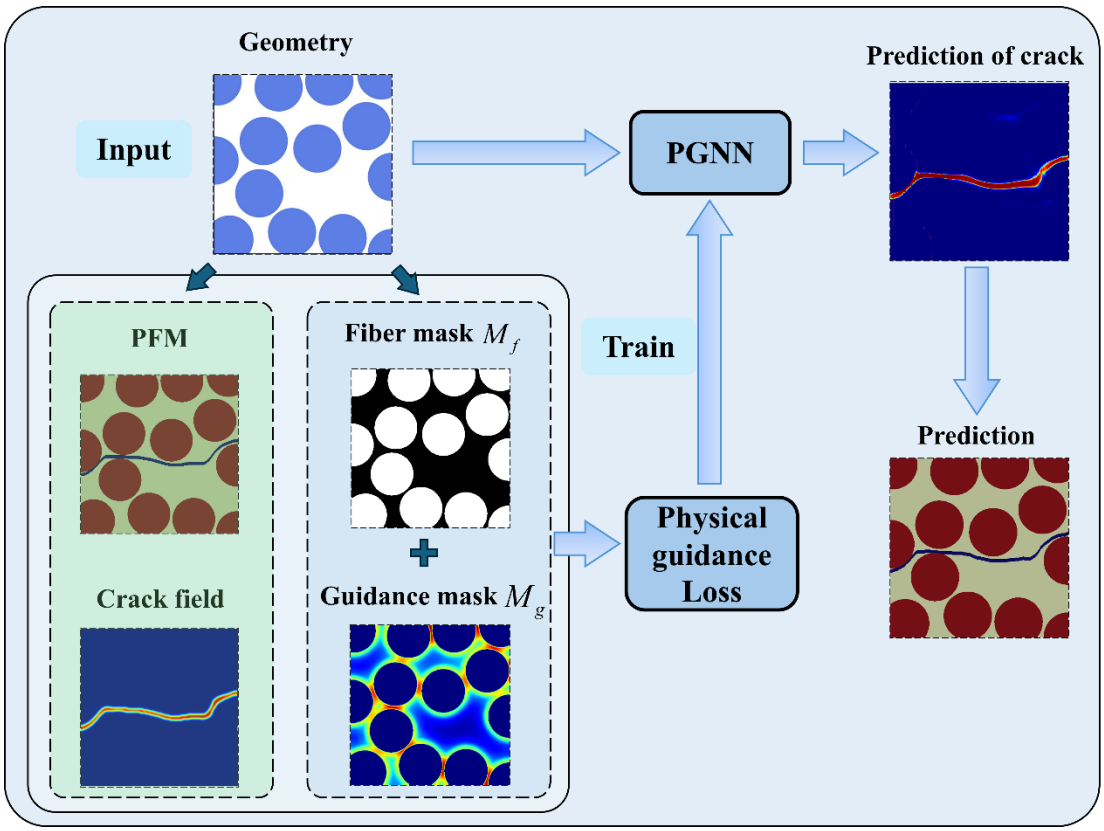

Fig. 3. Crack path prediction workflow.

A guidance mask M_g was then constructed to identify crack prone inter fiber matrix regions. As discussed in Section 2.3, tensile stress concentration and crack initiation are mainly observed in narrow matrix regions between closely spaced neighboring fibers, particularly when the center-to-center line of the corresponding fiber pair is approximately aligned with the tensile loading direction. These matrix regions were therefore marked in and used as mechanically preferred regions in the physical constraint loss.

Fig. 3 illustrates the microstructure image processing and crack path prediction workflow. It should be emphasized that M_f and M_g were not provided as additional input channels to the network. They were generated automatically during preprocessing and were used only to construct the physical constraint loss during training. Therefore, the network input remained a three channel microstructural image with a size of 3×512 ×512, while the target was a single channel phase field damage map with a size of 1× 512×512.

The dataset was randomly divided into training, validation, and testing subsets. The training set was used to update the network parameters, the validation set was used to monitor convergence and reduce overfitting, and the testing set was reserved for evaluating the prediction capability of the trained model. The dataset information is summarized in Table 1.

Table1

Dataset for PGNN model.

Data set	V_f(%)	Total(s)
Train	50-62	807
Validation	50-62	102
Test	50-62	102

3.2 Model architecture

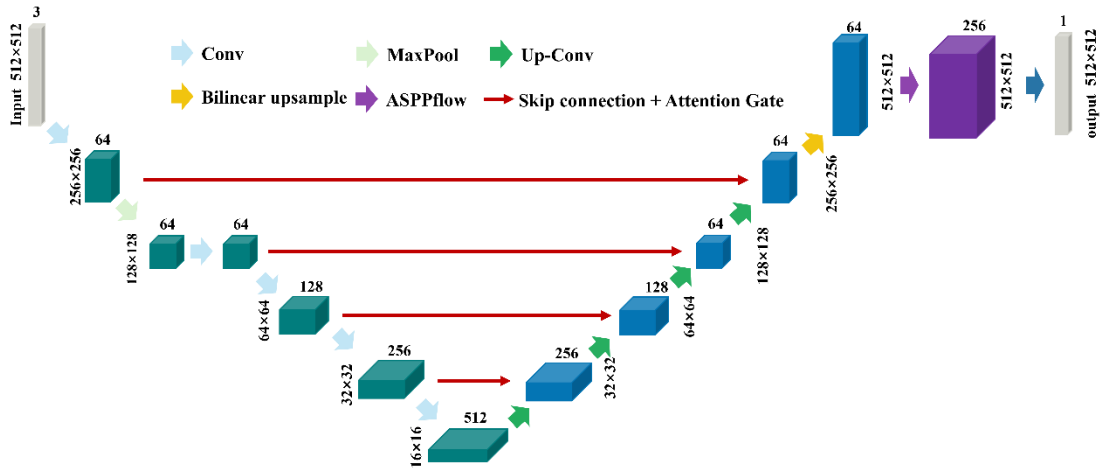

Fig. 4. Attention- ResNet architecture for predicting crack paths.

The architecture of the proposed PGNN is shown in Fig. 4. The network follows an encoder decoder structure to predict transverse crack paths as dense pixelwise fields. The encoder extracts multilevel microstructural features, and the decoder reconstructs the crack probability map by progressively restoring the spatial resolution [27].

ResNet34 was adopted as the encoder backbone, where residual connections facilitate gradient propagation and improve deep feature extraction [26]. The initial convolution layer captures low level geometric features, including fiber boundaries, matrix regions, and local fiber spacing. The subsequent residual stages gradually reduce the spatial resolution and increase the channel number, allowing higher level features related to fiber arrangement and potential crack paths to be extracted. For a 512×512 input image, the deepest encoder feature map has a spatial resolution of 16×16 and contains 512 channels.

A dilated convolution based multiscale module was introduced at the bottleneck to enlarge the receptive field without further reducing the feature resolution. Parallel convolutions with different dilation rates were used to aggregate local and contextual information [34], which is beneficial for capturing both fine crack segments between neighboring fibers and longer range crack continuity within the microstructural window.

The decoder consists of successive up convolution blocks. At each decoding level,

the upsampled feature map is fused with the corresponding encoder feature map through an attention gated skip connection. The skip connections preserve spatial details lost during downsampling [27], while the attention gates suppress less relevant responses before feature fusion [28]. This design helps retain the thin and tortuous morphology of transverse cracks while reducing redundant information from fiber interiors and background regions.

Let x_l denote the skip connection feature map from the encoder and g denote the gating signal from a coarser decoder layer. The attention coefficient is calculated as [28]

$$q_{\text{att}} = \psi^T\{\sigma_1(W_x^T x_l + W_g^T g + b_g)\} \tag{13}$$

$$\alpha = \sigma_2(q_{\text{att}}), \quad \hat{x}_l = \alpha \odot x_l, \tag{14}$$

where σ_1 is the ReLU activation function, σ_2 is the sigmoid function, W_x, W_g and ψ are linear transformations implemented by 1×1 convolutions, and denotes elementwise multiplication. The gated encoder features are then fused with the decoder features. A final 1×1 convolution is used to generate the single channel crack probability map.

3.3 Physics-guided loss function and training strategy

The proposed PGNN was trained by minimizing a composite loss function consisting of a supervised segmentation term and a physics-guided soft constraint term [35]. The crack path prediction task was formulated as a pixel-level binary classification problem, where the network outputs a crack probability map. Considering the strong imbalance between crack and non-crack pixels, a weighted binary cross-entropy loss was adopted as the primary supervised loss [36]. The total loss is defined as:

$$L_{\text{total}} = \lambda_{\text{BCE}} L_{\text{WBCE}} + \lambda_{\text{phys}} L_{\text{phys}} \tag{15}$$

Where L_{WBCE} and L_{phys} denote the weighted binary cross-entropy loss and the physics-guided loss, respectively. The coefficients λ_{BCE} and λ_{phys} balance the supervised segmentation term and the physics-guided constraint term.

The weighted binary cross-entropy loss is expressed as

$$L_{\text{WBCE}} = -\frac{1}{N}\sum_{i=1}^{N}\left[w_p y_i \log(\hat{y}_i + C) + (1 - y_i)\log(1 - \hat{y}_i + C)\right] \tag{16}$$

where N is the total number of pixels, $y_i \in \{0,1\}$ is the binary crack label at pixel i derived from the thresholded phase-field damage map, and $\hat{y}_i \in [0,1]$ is the predicted crack probability. Specifically, $y_i = 1$ denotes a crack pixel, whereas $y_i = 0$ denotes a non-crack pixel. In addition, w_p is the positive class weight assigned to crack pixels, and C is a small constant introduced for numerical stability. The coefficient w_p

increases the penalty for misclassified crack pixels and alleviates the bias toward the dominant background class [36].

The physics-guided loss consists of a fiber exclusion term and a crack-path guidance term:

$$L_{\text{phys}} = \lambda_f L_{\text{fiber}} + \lambda_g L_{\text{guide}} \tag{17}$$

where L_{fiber} penalizes crack probability inside fiber interiors, L_{guide} encourages the predicted crack probability to be concentrated in mechanically preferred inter-fiber matrix gaps, λ_f and λ_g control the relative contributions of the two physical terms. The fiber exclusion term is defined as

$$L_{\text{fiber}} = \frac{\sum_i \hat{y}_i M_{f,i}}{\sum_i M_{f,i} + C} \tag{18}$$

where $M_{f,i}$ is the fiber mask, with $M_{f,i} = 1$ for fiber pixels and $M_{f,i} = 0$ for matrix pixels. This term suppresses unphysical crack predictions inside fibers, which is consistent with the assumption that transverse damage mainly develops through matrix cracking and fiber-matrix interfacial damage rather than fiber breakage.

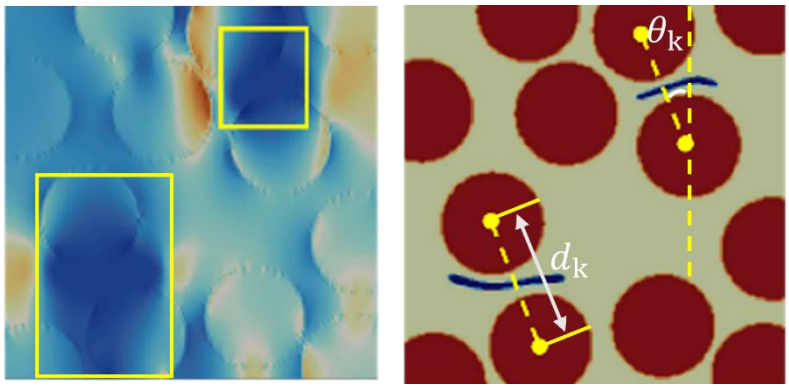

Fig. 5. Schematic of parameters d_k and θ_k in the physics-guided loss term.

To incorporate microstructure-based physical prior information, a continuous guidance map G was constructed from the fiber distribution. As shown in Fig 5. neighboring fiber pairs were first identified from the fiber mask, and each neighboring pair defined a candidate inter-fiber matrix gap. For the $k-th$ neighboring fiber pair, a physical preference weight s_k was assigned according to the spacing and orientation of the pair

$$s_k = f_d(d_k) f_\theta(\theta_k) \tag{19}$$

where d_k is the center-to-center distance between the two neighboring fibers, and θ_k is the acute angle between the center-to-center line and the loading direction. The function $f_d(d_k)$ decreases with increasing d_k, indicating that a shorter center-to-center distance corresponds to a narrower matrix gap and a higher cracking tendency.

The function $f_\theta(\theta_k)$ decreases with increasing θ_k, indicating that matrix gaps more aligned with the loading direction are assigned higher preference weights.

In this work, the physical preference weight was calculated as

$$s_k = \exp\left[-\frac{d_k - d_{\min}}{\tau_d}\right]\cos^2\theta_k \tag{20}$$

Where $d_{\min}$ is the minimum center-to-center distance among neighboring fiber pairs in the same RVE, and τ_d is a distance decay parameter. The exponential term assigns higher weights to narrower inter-fiber gaps, while the orientation term assigns higher weights to fiber pairs more aligned with the loading direction.

The continuous guidance map was obtained by accumulating the weighted candidate gap regions and normalizing the result

$$G_i = \mathrm{norm}\left(\sum_k s_k R_{k,i}\right) \tag{21}$$

where $R_{k,i}$ denotes the candidate matrix gap region associated with the $k-th$ neighboring fiber pair. Specifically, $R_{k,i}=1$ when pixel i belongs to the corresponding inter-fiber matrix gap, and $R_{k,i}=0$ otherwise. The operator $\mathrm{norm}(\cdot)$ maps the accumulated guidance field to $[0,1]$. Owing to this weighted normalization, the guidance map is dominated by mechanically critical matrix gaps with smaller spacing and more favorable orientation, rather than treating all neighboring gaps equally.

Based on the guidance map, the crack-path guidance loss is defined as

$$L_{\mathrm{guide}} = 1 - \frac{\sum_i \hat{y}_i G_i (1 - M_{f,i})}{\sum_i \hat{y}_i (1 - M_{f,i}) + C} \tag{22}$$

This term measures the normalized physical preference accumulated by the predicted crack probability in matrix regions. The numerator represents the weighted overlap between the predicted crack probability and the high-preference inter-fiber matrix gaps, while the denominator represents the total predicted crack probability in the matrix region. A lower value of L_{guide} indicates that the predicted crack probability is more concentrated in matrix gaps with higher physical preference weights.

It should be noted that L_{guide} was used as a soft physical constraint rather than a hard restriction on the crack path. The network was not forced to generate cracks only within high-preference regions. Instead, the guidance term reduced the loss when the predicted crack probability overlapped with mechanically favorable inter-fiber matrix gaps. Therefore, crack deflection, coalescence, and local path variation were still learned from the binary crack labels derived from the phase-field damage maps through the supervised loss, while the physical guidance term provided additional

microstructure-based prior information.

The model was implemented in PyTorch and trained on an NVIDIA GeForce RTX 5070 GPU. Model parameters were optimized using the AdamW optimizer, with an initial learning rate of 1×10^{-3} and a weight decay of 1×10^{-4}. A ReduceLROnPlateau scheduler was adopted to adaptively adjust the learning rate. If the validation loss did not decrease for 4 consecutive epochs, the learning rate was reduced by a factor of 0.5. The model was trained for 30 epochs with a batch size of 4. The evolution of training and validation losses was recorded to evaluate convergence and identify potential overfitting.

4. Sequential prediction of crack paths based on transfer learning

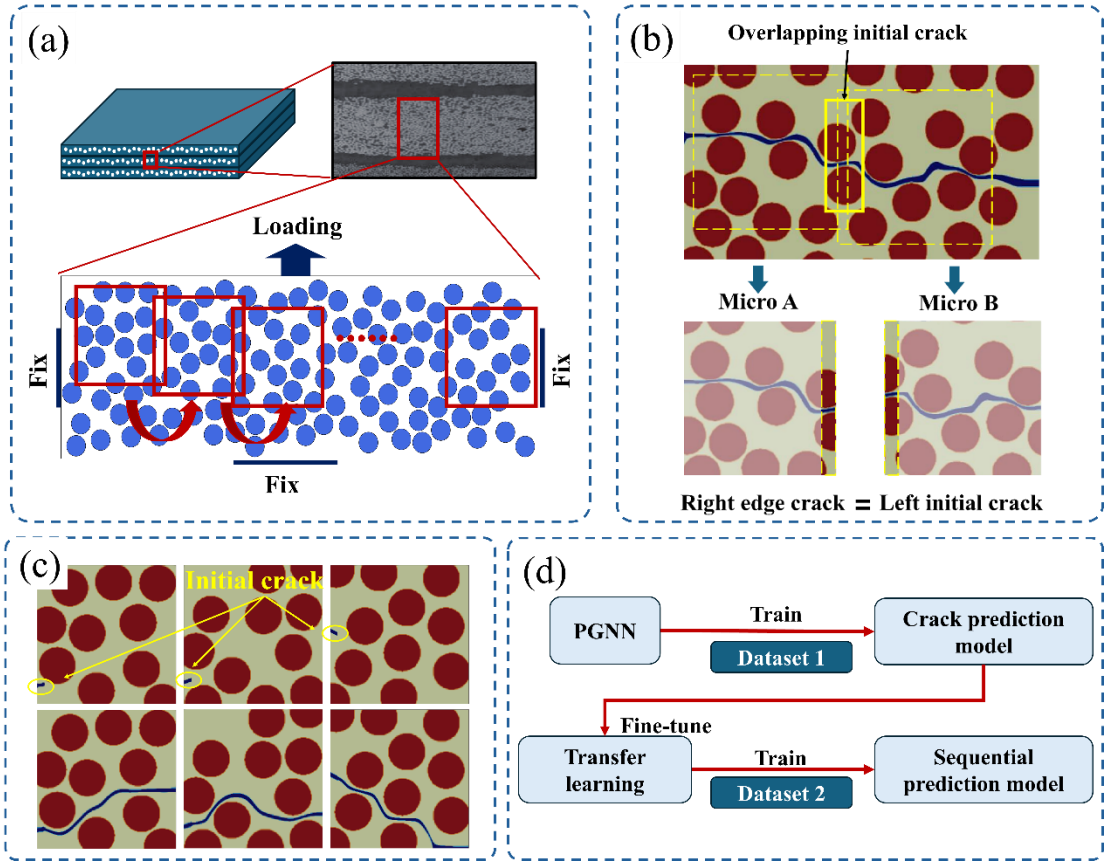

Fig. 6. Sequential crack path prediction strategy. (a) Decomposition of the crack path into a series of microstructural windows. (b) Crack-state transfer via an inherited initial crack. (c) Selected phase-field results from the dataset with predefined initial cracks. (d) Transfer learning workflow for adapting the pretrained PGNN to the initial-crack-conditioned prediction.

A sequential prediction strategy was developed to extend the proposed microstructure-level model from isolated windows to a larger crack propagation region. As schematically shown in Fig. 6(a), the crack path prediction in a single CFRP ply can be decomposed into a series of $30\,\mu m\times30\,\mu m$ microstructural windows along the nominal propagation direction. If these windows are predicted independently, the

resulting crack segments remain isolated and the influence of the previously formed crack on subsequent propagation cannot be considered. To address this issue, an inherited initial crack was introduced to link adjacent windows. Specifically, the crack segment at the right boundary of the previous prediction was inserted into the left boundary of the next window as the initial crack, as illustrated in Fig. 6(b). This operation enables crack-state transfer between neighboring windows and allows the local predictions to be connected into a continuous crack path.

Fig. 6(d) illustrates the transfer learning workflow employed to adapt the pretrained PGNN to the initial-crack conditioned prediction task. The model trained on intact microstructural windows (Section 3.3) served as the source model, and its learned weights were loaded as the initial parameters of the target model. The encoder backbone was frozen for the first three epochs to retain the low-level and multiscale microstructural features learned from the source dataset. It was then unfrozen, and the entire network was fine-tuned using the initial-crack dataset. AdamW was employed with a reduced learning rate, and a ReduceLROnPlateau scheduler adjusted the learning rate according to the validation loss. The model with the best validation performance was used for sequential crack path prediction.

Table2

Dataset for Sequential prediction model.

Data set	V_f(%)	Total(s)
Train	50-62	641
Validation	50-62	80
Test	50-62	80

This strategy links neighboring prediction windows through the inherited crack segment, allowing the fine-tuned PGNN to account for both the local fiber distribution and the crack state transferred from the preceding window. Therefore, continuous transverse crack paths can be reconstructed recursively over larger microstructural domains.

5. Results and discussion

5.1 Results of the PGNN model for transverse crack

Two representative microstructural samples with different fiber distributions were selected to evaluate the effect of the attention mechanism and the physics-guided loss. Fig. 7(a) compares the crack paths predicted by the conventional U-Net and the proposed PGNN with the phase-field reference results.

The U-Net model captured the overall trend of crack propagation after training on the microstructure–phase-field dataset. However, the enlarged views reveal clear local deviations. In several regions, the predicted crack path passed through fiber interiors or

deviated from the dominant matrix crack trajectory. This limitation became more evident in microstructures with complex fiber distributions, indicating that the conventional U-Net had insufficient ability to distinguish physically admissible crack paths.

The proposed PGNN produced crack paths that were more consistent with the phase-field results. The predicted cracks mainly propagated through matrix regions and avoided fiber interiors, which agrees with the transverse cracking mechanism of CFRP composites. For samples with complex fiber arrangements, the proposed model also captured crack deflection and local path variation more accurately. This improvement is attributed to the attention-enhanced encoder–decoder architecture and the physics-guided loss. The attention mechanism strengthens multiscale feature extraction and improves the correlation between fiber distribution and crack morphology, while the physics-guided loss introduces constraints related to fiber exclusion and inter-fiber cracking tendency.

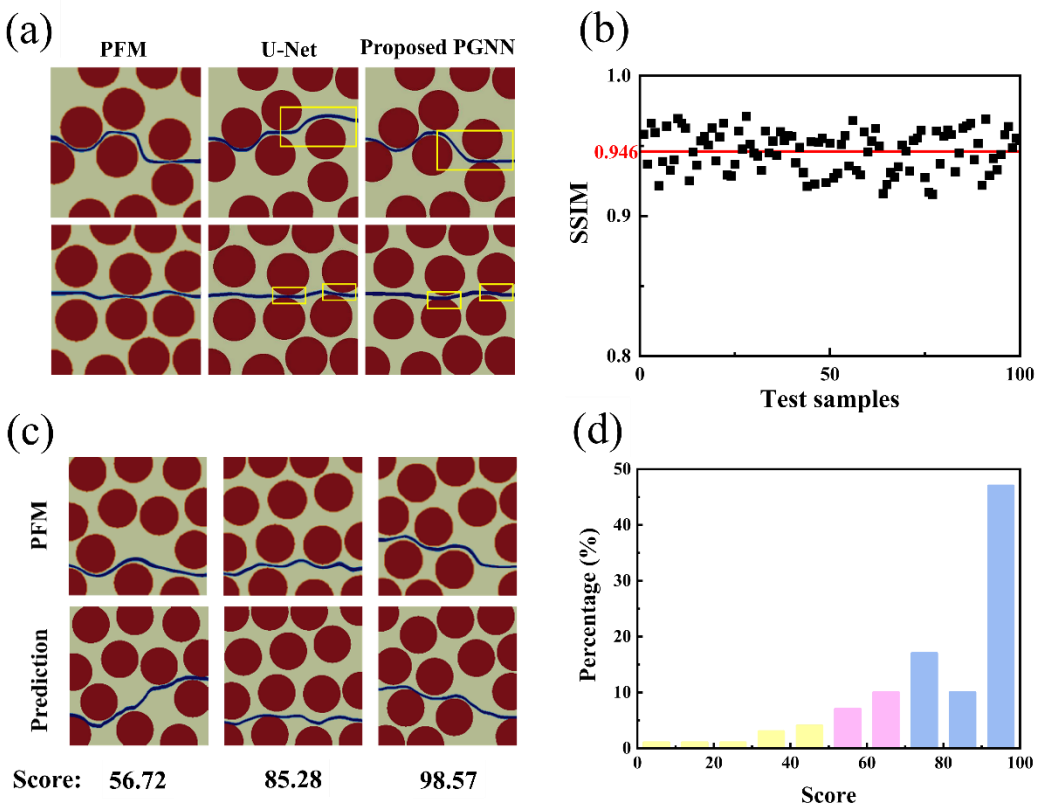

Fig. 7. Performance evaluation of the proposed PGNN for crack path prediction. (a) Comparison of predicted crack paths with phase-field references for two microstructures. (b) SSIM distribution of 102 test samples. (c) Representative cases with different crack score levels. (d) Statistical distribution of crack scores over the test set.

The structural similarity index measure (SSIM) was used to quantify the agreement between the predicted crack field and the phase-field reference result [29].

SSIM evaluates image similarity in terms of luminance, contrast, and structural information, and is defined as

$$\mathrm{SSIM}(x,y)=\frac{(2\mu_x\mu_y+C_1)(2\sigma_{xy}+C_2)}{(\mu_x^2+\mu_y^2+C_1)(\sigma_x^2+\sigma_y^2+C_2)} \tag{23}$$

where x and y are the predicted crack field and the phase-field reference result, respectively. μ_x and μ_y denote the mean intensities, σ_x^2 and σ_y^2 denote the variances, and σ_{xy} is the covariance between the two images. C_1 and C_2 are stabilization constants, commonly defined as $C_1=(K_1L)^2$ and $C_2=(k_2L)^2$, where L is the image dynamic range, K_1 and K_2 are empirical constants [29].

Fig. 7(b) presents the SSIM distribution of 102 test samples. The minimum SSIM was 0.931, and the average value reached 0.946. The high SSIM values indicate that the proposed model reproduced the phase-field crack fields with strong structural agreement. The narrow distribution also suggests stable prediction performance for different random fiber arrangements.

A modified Hausdorff-distance-based crack score was further introduced to provide a path-sensitive evaluation [30]. Unlike SSIM, which measures global image similarity, this score directly evaluates the agreement between the predicted and reference crack paths. The score was normalized to $0-100$, with a higher value indicating better path consistency. Representative cases with different score levels are shown in Fig. 7(c). Scores below 60 correspond to large path deviations or limited overlap with the reference crack. Scores between 60 and 80 indicate similar overall propagation directions but noticeable local differences. Scores above 80 represent high agreement between the predicted and phase-field crack paths.

Fig. 7(d) shows the statistical distribution of crack scores over the test set. Only 9.9% of the predictions scored below 60, while 74.3% achieved scores above 70. These results confirm that the proposed model provides reliable crack path predictions at both the image-field and path levels. The combined SSIM and crack score analyses demonstrate the accuracy and generalization capability of the physics-guided model for microstructure-level transverse crack prediction.

5.2 Results of the transfer learning model for crack sequential prediction

Three representative microstructures containing predefined initial cracks were selected to assess the transfer learning model, as shown in Fig. 8(a). The model accurately recognized the initial crack embedded at the left boundary and predicted subsequent crack propagation from this inherited crack state. The predicted trajectories were consistent with the phase-field reference results, indicating that transfer learning enabled the model to capture the effect of the initial crack on local crack evolution.

Fig. 8(b) compares the SSIM before and after transfer learning, and Fig. 8(c)

compares the crack score. Both metrics improved after fine-tuning on the initial-crack dataset. The average SSIM increased to 0.959, and 80.2% of the samples achieved crack scores above 70. These improvements indicate that the pretrained model retained useful microstructure-dependent crack features from the source task, while fine-tuning adapted the model to the initial-crack-conditioned prediction task.

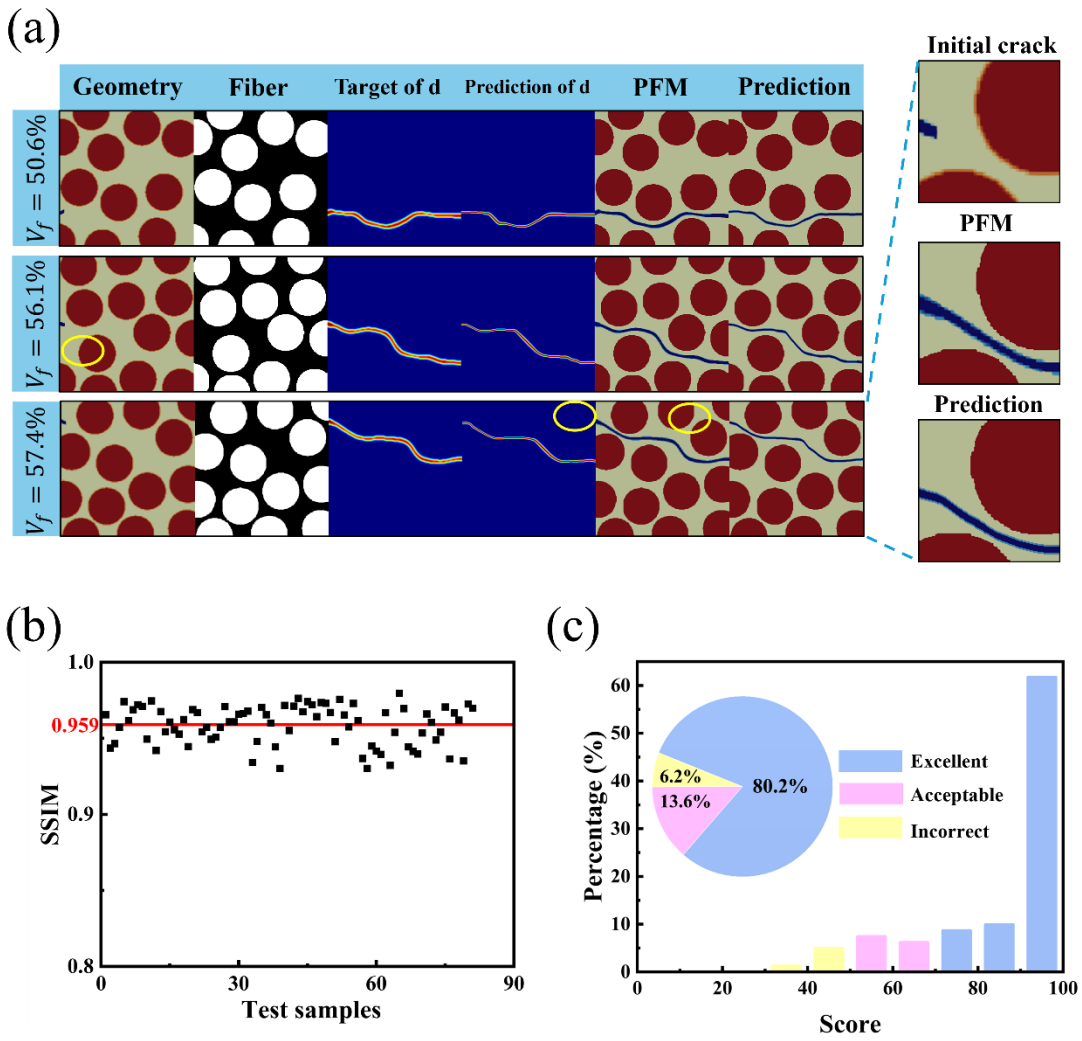

Fig. 8. Evaluation of the transfer learning model for Sequential prediction. (a) Predicted crack paths for three representative microstructures with predefined initial cracks. (b) Comparison of SSIM before and after transfer learning. (c) Comparison of crack scores before and after transfer learning.

An extended microstructure with a length of 200 μm and a width of 50 μm was generated to examine the feasibility of sequential crack path prediction. This case represents transverse matrix cracking in a continuous fiber-reinforced composite region. As shown in Fig. 9(a), the extended microstructure was divided into smaller prediction windows compatible with the neural network input size, while maintaining spatial continuity between adjacent windows. The corresponding phase-field simulation result was used as the reference crack path.

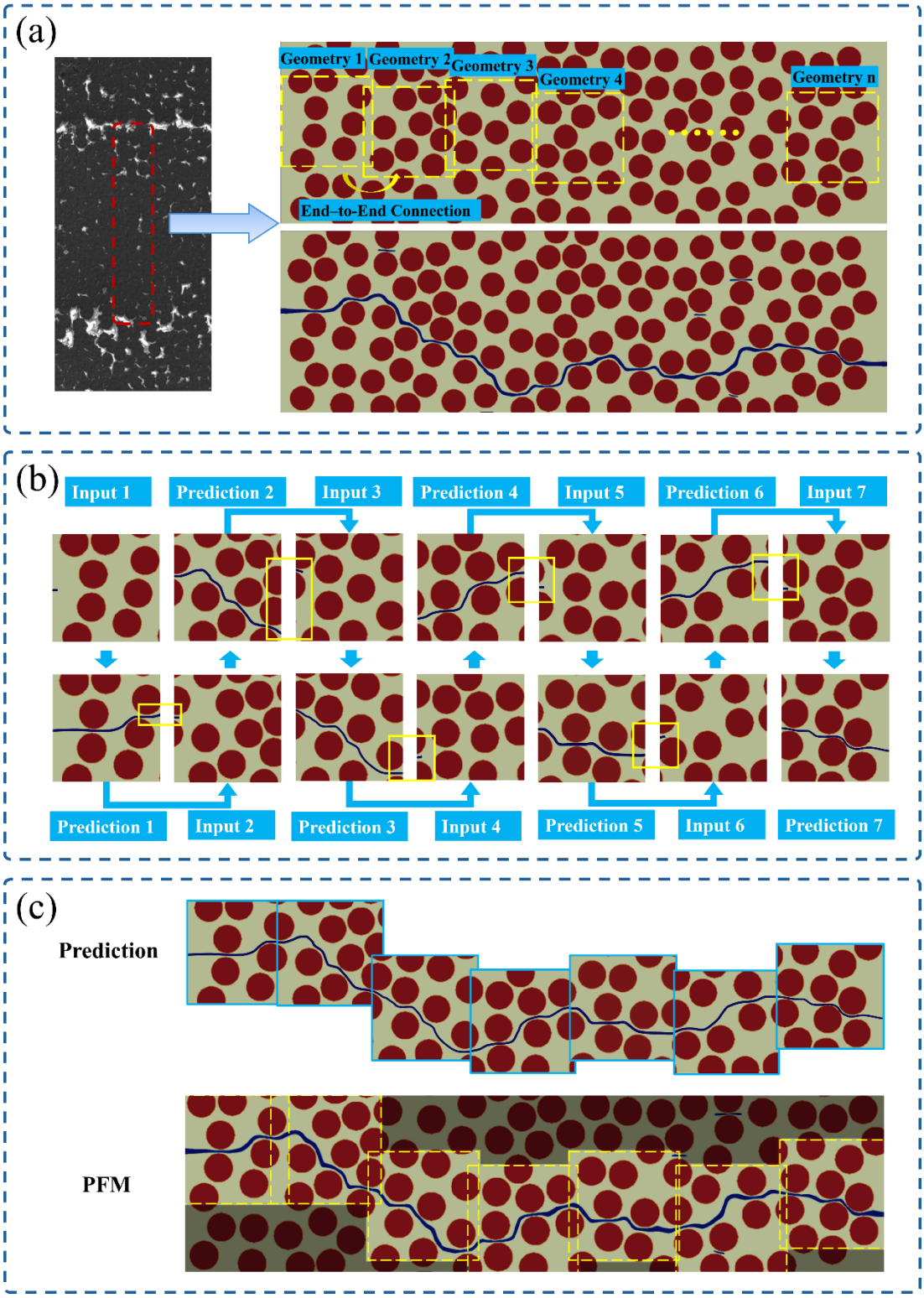

Fig. 9. Sequential crack path prediction over an extended microstructure. (a) Partitioning of the extended microstructure into prediction windows and the phase-field reference. (b) Schematic of the sequential prediction procedure. (c) Stitched prediction versus phase-field reference.

Fig. 9(b) illustrates the sequential prediction process. A crack-prone region on the left side of the extended microstructure was first selected as the initial prediction

window. The model described in Section 3.3 was applied to this window to obtain the first predicted crack field. The crack segment at the right boundary of this prediction was then transferred to the left boundary of the next window as the inherited initial crack. The next window was predicted using the transfer-learning model. This operation was repeated until the crack path over the entire extended microstructure was reconstructed.

The stitched prediction is compared with the phase-field result in Fig. 9(c). The proposed sequential strategy accurately predicted the crack path within each local window and maintained crack continuity between neighboring windows through the inherited initial crack. The reconstructed path closely followed the phase-field reference result, demonstrating that the proposed framework can extend crack path prediction from a 30 μm local window to a 200 μm extended microstructural region. The prediction time was reduced to the millisecond level, indicating a substantial improvement in computational efficiency compared with phase-field fracture simulation. These results demonstrate the potential of the proposed framework as an efficient surrogate model for continuous transverse crack path prediction in CFRP composites.

6. Conclusions

This study presents a physics-guided deep learning framework for sequential prediction of transverse crack paths in carbon fiber-reinforced polymer (CFRP) composites. Phase-field fracture simulations were first performed to investigate the micro-mechanisms of crack initiation and propagation under transverse loading. Building upon the revealed mechanisms, an attention-enhanced encoder – decoder network incorporating physical guidance was proposed. A sequential prediction strategy, which introduces inherited initial crack information and transfer learning, was then established to extend local crack path predictions to continuous paths over extended microstructural regions. The main conclusions are summarized as follows:

1. Phase-field analysis revealed that fiber distribution directly governs crack initiation. A shorter distance between adjacent fibers and a smaller angle between the line connecting their centers and the loading direction intensify stress concentration in the matrix-rich inter-fiber region, thereby facilitating crack nucleation.

2. A physics guided neural network was developed, in which geometric features of neighboring fibers, including relative position, fiber spacing, and center connection angle, are incorporated into the loss function as physical constraints. This guidance improves crack path prediction accuracy. Evaluations using SSIM and a modified Hausdorff distance show high structural consistency with phase field results, achieving a prediction accuracy of 93.8%.

3. By introducing inherited initial crack information, the framework establishes

crack-state transfer between adjacent microstructural windows, enabling the model to infer continuous crack propagation from local historical states. This sequential prediction scheme overcomes the limitation of conventional data-driven methods in connecting isolated crack segments into coherent paths.

Compared with traditional phase field and finite element simulations that require iterative nonlinear solvers, the proposed framework achieves millisecond inference per window, representing orders-of-magnitude acceleration. This efficiency provides a basis for concurrent multiscale analysis and rapid failure assessment of composite structures. The framework offers a promising surrogate for transverse crack prediction and can be extended to three-dimensional microstructures and more complex loading conditions.

References

[1] J. Zhang, G. Lin, U. Vaidya, H. Wang, Past, present and future prospective of global carbon fibre composite developments and applications, Compos. Part B Eng. 250 (2023) 110463, https://doi.org/10.1016/j.compositesb.2022.110463.

[2] D.J. Mortell, D.A. Tanner, C.T. McCarthy, In-situ SEM study of transverse cracking and delamination in laminated composite materials, Compos. Sci. Technol. 105 (2014) 118–126, https://doi.org/10.1016/j.compscitech.2014.10.012.

[3] R. Talreja, Transverse cracking and stiffness reduction in composite laminates, J. Compos. Mater. 19 (1985) 355–375, https://doi.org/10.1177/002199838501900404.

[4] R. Talreja, Stiffness properties of composite laminates with matrix cracking and interior delamination, Eng. Fract. Mech. 25 (1986) 751–762, https://doi.org/10.1016/0013-7944(86)90038-X.

[5] S.E. Groves, C.E. Harris, A.L. Highsmith, D.H. Allen, R.G. Norvell, An experimental and analytical treatment of matrix cracking in cross-ply laminates, Exp. Mech. 27 (1987) 73–79, https://doi.org/10.1007/BF02318867.

[6] P. Ladevèze, O. Allix, J.F. Deü, D. Lévêque, A mesomodel for localisation and damage computation in laminates, Comput. Methods Appl. Mech. Eng. 183 (2000) 105–122, https://doi.org/10.1016/S0045-7825(99)00214-5.

[7] D. Han, F. Ye, L. Cheng, Y. Zhang, Y. Wei, J. Zhang, Matrix cracking of 2D SiC/SiC composite characterized by in situ SEM and nano-CT, Ceram. Int. 49 (2023) 12508–12517, https://doi.org/10.1016/j.ceramint.2022.12.111.

[8] Y. Sheng, D. Yang, Y. Tan, J. Ye, Microstructure effects on transverse cracking in composite laminae by DEM, Compos. Sci. Technol. 70 (2010) 2093–2101, https://doi.org/10.1016/j.compscitech.2010.08.006.

[9] A. El Moumen, T. Kanit, A. Imad, Numerical evaluation of the representative volume element for random composites, Eur. J. Mech. A/Solids 86 (2021) 104181, https://doi.org/10.1016/j.euromechsol.2020.104181.

[10] B. Wang, K. Huang, L. Guo, A two-stage deep learning framework for predicting crack patterns and mechanical properties of unidirectional composites with void defects, Compos. Sci. Technol. 271 (2025) 111357, https://doi.org/10.1016/j.compscitech.2025.111357.

[11] S.C. Garcea, Y. Wang, P.J. Withers, X-ray computed tomography of polymer composites, Compos. Sci. Technol. 156 (2018) 305–319, https://doi.org/10.1016/j.compscitech.2017.10.023.

[12] B. Yu, R.S. Bradley, C. Soutis, P.J. Hogg, P.J. Withers, A comparison of different approaches for imaging cracks in composites by X-ray microtomography, Philos. Trans. R. Soc. A 374 (2016) 20160037, https://doi.org/10.1098/rsta.2016.0037.

[13] D. Grogan, C. Ó Brádaigh, S. Leen, A combined XFEM and cohesive zone model for composite laminate microcracking and permeability, Compos. Struct. 120 (2015) 246–261, https://doi.org/10.1016/j.compstruct.2014.09.068.

[14] M. Joosten, M. Dingle, A.P. Mouritz, A.A. Khatibi, S. Agius, C.H. Wang, A hybrid embedded cohesive element method for predicting matrix cracking in composites, Compos. Struct. 136 (2016) 554–565, https://doi.org/10.1016/j.compstruct.2015.10.030.

[15] P. Zhang, X. Hu, T.Q. Bui, W. Yao, Phase field modeling of fracture in fiber reinforced composite laminate, Int. J. Mech. Sci. 161–162 (2019) 105008, https://doi.org/10.1016/j.ijmecsci.2019.07.007.

[16] W. Tan, E. Martínez-Pañeda, Phase field predictions of microscopic fracture and R-curve behaviour of fibre-reinforced composites, Compos. Sci. Technol. 202 (2021) 108539, https://doi.org/10.1016/j.compscitech.2020.108539.
[17] Y. Lu, Y. Feng, W. Huang, Z. Su, Y.E. Ma, S. Wang, A multiscale modeling for progressive failure behavior of unidirectional fiber-reinforced composites based on phase-field method, Eng. Fract. Mech. 310 (2024) 110517, https://doi.org/10.1016/j.engfracmech.2024.110517.
[18] P. Zhang, K. Tang, G. Chen, J. Li, Y. Li, Multimodal data fusion enhanced deep learning prediction of crack path segmentation in CFRP composites, Compos. Sci. Technol. 257 (2024) 110812, https://doi.org/10.1016/j.compscitech.2024.110812.
[19] X. Peng, Q. Yao, B. Yi, J. Xie, J. Li, S. Jiang, Deep learning approach for predicting multi-component stress fields in fiber-reinforced composites under different load paths, Compos. Sci. Technol. 268 (2025) 111198, https://doi.org/10.1016/j.compscitech.2025.111198.
[20] Z. Gu, X. Kong, J. Liu, X. Ding, X. Hou, A coupled deep learning and DEM modelling approach for transverse crack prediction in UD-GFRP composites, Compos. Sci. Technol. 269 (2025) 111234, https://doi.org/10.1016/j.compscitech.2025.111234.
[21] M. Li, B. Wang, J. Hu, G. Li, P. Ding, C. Ji, B. Wang, Artificial neural network-based homogenization model for predicting multiscale thermo-mechanical properties of woven composites, Int. J. Solids Struct. 292 (2024) 112965, https://doi.org/10.1016/j.ijsolstr.2024.112965.
[22] S.K. Maharana, G. Soni, M. Mitra, A machine learning-based prediction of biaxial failure envelope of a short fiber-reinforced polymer composite, Compos. Sci. Technol. 267 (2025) 111176, https://doi.org/10.1016/j.compscitech.2025.111176.
[23] H. Xu, W. Fan, L. Ruan, R. Shi, C.T. Ambrose, D. Zhang, Crack-Net: A deep learning approach to predict crack propagation and stress–strain curves in particulate composites, Engineering 49 (2025) 149–163, https://doi.org/10.1016/j.eng.2025.02.022.
[24] X. Ma, X. He, Z.C. Tu, Prediction of fatigue–crack growth with neural network-based increment learning scheme, Eng. Fract. Mech. 241 (2021) 107402, https://doi.org/10.1016/j.engfracmech.2020.107402.
[25] P. Zhang, Y. Xiang, K. Tang, Deep learning surrogate for phase field modeling in fiber-reinforced composites: From stress evolution to final crack path, Comput. Methods Appl. Mech. Eng. 448 (2026) 118518, https://doi.org/10.1016/j.cma.2025.118518.
[26] K. He, X. Zhang, S. Ren, J. Sun, Deep residual learning for image recognition, in: Proc. IEEE Conf. Comput. Vis. Pattern Recognit., 2016, pp. 770–778, https://doi.org/10.1109/CVPR.2016.90.
[27] O. Ronneberger, P. Fischer, T. Brox, U-Net: convolutional networks for biomedical image segmentation, in: Medical Image Computing and Computer-Assisted Intervention – MICCAI 2015, Lecture Notes in Computer Science, vol. 9351, Springer, Cham, 2015, pp. 234–241, https://doi.org/10.1007/978-3-319-24574-4_28.
[28] O. Oktay, J. Schlemper, L. Le Folgoc, M. Lee, M. Heinrich, K. Misawa, et al., Attention U-Net: learning where to look for the pancreas, arXiv:1804.03999, 2018, https://doi.org/10.48550/arXiv.1804.03999.
[29] Z. Wang, A.C. Bovik, H.R. Sheikh, E.P. Simoncelli, Image quality assessment: from error visibility to structural similarity, IEEE Trans. Image Process. 13 (2004) 600–612, https://doi.org/10.1109/TIP.2003.819861.
[30] M.P. Dubuisson, A.K. Jain, A modified Hausdorff distance for object matching, in: Proc. 12th Int. Conf. Pattern Recognition, 1994, pp. 566–568, https://doi.org/10.1109/ICPR.1994.576361.

[31] J.J. Espadas-Escalante, N.P. van Dijk, P. Isaksson, A phase-field model for strength and fracture analyses of fiber-reinforced composites, Compos. Sci. Technol. 174 (2019) 58–67, https://doi.org/10.1016/j.compscitech. 2018.10.031 .

[32] C. Miehe, L.-M. Schänzel, H. Ulmer, Phase field modeling of fracture in multi-physics problems. Part I. Balance of crack surface and failure criteria for brittle crack propagation in thermo-elastic solids, Comput. Methods Appl. Mech. Eng. 294 (2015) 449–485, https://doi.org/10.1016/j.cma.2014.11.016.

[33] D. Gaston, C. Newman, G. Hansen, D. Lebrun-Grandie, MOOSE: A parallel computational framework for coupled systems of nonlinear equations, Nucl. Eng. Des. 239 (2009) 1768–1778, https://doi.org/10.1016/j.nucengdes.2009.05.021.

[34] L.-C. Chen, G. Papandreou, I. Kokkinos, K. Murphy, A.L. Yuille, DeepLab: semantic image segmentation with deep convolutional nets, atrous convolution, and fully connected CRFs, IEEE Trans. Pattern Anal. Mach. Intell. 40 (2018) 834–848, https://doi.org/10.1109/TPAMI.2017.2699184.

[35] M. Raissi, P. Perdikaris, G.E. Karniadakis, Physics-informed neural networks: a deep learning framework for solving forward and inverse problems involving nonlinear partial differential equations, J. Comput. Phys. 378 (2019) 686–707, https://doi.org/10.1016/j.jcp.2018.10.045.

[36] Q.D. Nguyen, H.-T. Thai, Crack segmentation of imbalanced data: the role of loss functions, Eng. Struct. 297 (2023) 116988, https://doi.org/10.1016/j.engstruct.2023.116988.